Large-amplitude harmonic driving of highly coherent flux qubits

Alejandro Ferrón, Daniel Domínguez, and María José Sánchez
Centro Atómico Bariloche and Instituto Balseiro, 8400 San Carlos de Bariloche, Río Negro, Argentina
(Received 17 June 2010; revised manuscript received 24 September 2010; published 19 October 2010)

The device for the Josephson flux qubit can be considered as a solid-state artificial atom with multiple energy levels. When a large-amplitude harmonic excitation is applied to the system, transitions at the energy levels avoided crossings produce visible changes in the qubit population over many driven periods that are accompanied by a rich pattern of interference phenomena. We present a Floquet treatment of the periodically time-dependent Schrödinger equation of the strongly driven qubit beyond the standard two-level approach. For low amplitudes, the average probability of a given sign of the persistent current qubit exhibits, as a function of the static flux detuning and the driving amplitude, Landau-Zener-Stückelberg (LZS) interference patterns that evolve into complex diamondlike patterns for large amplitudes. In the case of highly coherent flux qubits we show that the higher-order diamonds can not be simply described relying on LZS transitions in each avoided crossing considered separately. In addition we propose a spectroscopic method based on starting the system in the first excited state instead of in the ground state, which can give further information on the energy-level spectrum and dynamics in the case of highly coherent flux qubits. We compare our numerical results with recent experiments that perform amplitude spectroscopy to probe the energy spectrum of the artificial atom.

DOI: 10.1103/PhysRevB.82.134522 PACS number(s): 74.50.+r, 85.25.Cp, 03.67.Lx, 42.50.Hz

I. INTRODUCTION

In recent years, several types of superconducting qubits have been experimentally studied.[1–5] These systems consist on mesoscopic Josephson devices and constitute promising candidates to be used for the design of qubits for quantum computation.[1–8] Indeed, a large effort is devoted to succeed in the coherent manipulation of their quantum states in a controllable way. The progress made along this line allows to have nowadays Josephson circuits with small dissipation and large decoherence times.[3,4,6–8]

In this work we will focus on the device for the Josephson flux qubit (DJFQ), which consists of a superconducting quantum interference device (SQUID) loop with three Josephson junctions operated at or near a magnetic flux of half quantum.[2,6–8] When cooling down to millikelvin temperatures this device exhibits quantized levels whose energies can be tuned by a control parameter such as an external magnetic field. This artificial atomlike behavior has motivated several studies based on the analysis of the level spectrum and its dynamics beyond the simplified two-level approach. As an example it has been shown that, after the inclusion of higher energy levels the DJFQ exhibits quantum signatures of classical chaos;[9,10] and a recent study[11] focused on the calculation of the intrinsic leakage (i.e., transitions from the allowed qubit states to higher excited levels of the system) has shown that for very strong resonant harmonic pulses the two-level approximation breaks down.

What is more important, several recent experiments driving the flux qubit with a combination of a dc and large-amplitude harmonic excitations in the magnetic flux have studied the energy-level structure through Landau-Zener-Stückelberg transitions.[12–15] Mach-Zender interferometry[13,14] and amplitude spectroscopy[15] have been the subject of these recent experimental studies of the flux qubit as an artificial atom. In particular, the amplitude spectroscopy experiment of Ref. 15 has revealed the higher energy level spectrum when increasing the microwave amplitude. In this case, the average population of one state of the DJFQ as a function of the dc flux (flux detuning) and microwave amplitude exhibits diamondlike interference patterns, which display a rich structure of multiphoton resonances.[13] From these interference patterns it is, in principle, possible to reconstruct a large fraction of the energy spectrum and methods based on two-dimensional Fourier transform have been recently proposed to this end.[16] In the experiment, the observed spectroscopic "diamonds" arise due to combined contributions of Landau-Zener-Stückelberg transitions, which provide the interference fingerprint of different energy-level avoided crossings, together with intrawell fast relaxation and short coherence times, which provide contrast in the observed pattern.

Recent theoretical efforts have been put forward to reconstruct the experimentally observed interference patterns by solving the dynamics of the model under strong driving. Most of the reported approaches reduce the model for the DJFQ to a simplified version which only considers the dynamics of the two levels involved in each avoided crossing. In this case the well-known Landau-Zener-Stückelberg theory has been applied, considering only the accumulated phase of the two levels during a period of the driving.[13,17] The beginning of the first spectroscopic diamond, that corresponds to the first avoided crossing, is accurately reproduced within this basic model.[13,17] Additionally, extensions that incorporate several levels based on rate equations along all coupled levels have been recently proposed.[18] In this later case more than one diamond can be obtained but the approach neglects the phase accumulated in the evolution of several levels and can only be applied when decoherence and relaxation effects are important. Since this case is somewhat near the experiment of Ref. 15, a qualitative description of the observed diamond patterns can be obtained. However, the devices for the flux qubit can have larger decoherence times[8,19] than in the case of Ref. 15. In this case, the effect of fast intrawell relaxation that provided contrast in the diamond patterns, and the effect of short decoherence times that

made possible to consider only the accumulated phases of two levels at the avoided crossings, will be much weaker. Then the question arises on how the interference patterns of strongly driven DJFQ can be analyzed in the highly coherent case and how much information on the energy spectrum can be extracted in this situation.

The purpose of this work is to solve the dynamics of the DJFQ under strong driving rf pulses considering the full Hamiltonian of the system. We perform a first-principles calculation taking as input only two parameters from the experimental device: the ratio of the Josephson and charging energies, E_J/E_C, and the asymmetry factor α of the Josephson energy of one of the junctions with respect to the others. Furthermore, our approach focus on the behavior of highly coherent DJFQ when driven within time scales smaller than the dephasing time. Therefore the interaction with the environment is neglected and we solve the time-dependent Schrödinger equation considering the DJFQ as a closed system. As we will show, even when relaxation and dephasing are neglected, our results reproduce several of the qualitative features of the experiment of Ref. 15.

We will employ the Floquet formalism[20] which has been extensively applied to study time-dependent periodic evolutions in systems ranging from two-level systems (TLSs), including simplified models of flux qubits,[21] to more realistic molecular and nanoscaled systems.[22] The Floquet method allows to transform the periodically time-dependent Schrödinger equation into an equivalent infinitely dimensional eigenvalue problem for a time-independent Floquet matrix. In general several truncations schemes are employed in order to tackle the analytical solution and reduce the infinite Floquet matrix to an effective finite-dimensional matrix.[23]

The paper is organized as follows. In Sec. II we introduce the model Hamiltonian and equations for the Josephson flux qubit. In Sec. III we present numerical results for the amplitude spectroscopy for the Josephson flux qubit by direct numerical calculation and using the Floquet formulation for the time-dependent Schrödinger equation in the case of an harmonic drive. In this section we compare our numerical results with recent experimental realizations. In Sec. IV we propose an amplitude spectroscopy method by changing the initial conditions. Numerical calculations using the Floquet formulation are presented. Finally, Sec. V contains a summary and a discussion of the most relevant points of our findings.

II. MODEL FOR THE DEVICE FOR THE JOSEPHSON FLUX QUBIT

The DJFQ consists on a superconducting ring with three Josephson junctions[2] enclosing a magnetic flux $\Phi=f\Phi_0$ with $\Phi_0=h/2e$, see Fig. 1.

The junctions have gauge invariant phase differences defined as φ_1, φ_2, and φ_3, respectively, with the sign convention corresponding to the directions indicated by the arrows in Fig. 1. Typically the circuit inductance can be neglected and the phase difference of the third junction is: $\varphi_3=-\varphi_1+\varphi_2-2\pi f$. Therefore the system can be described with two

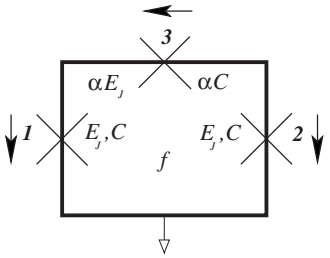

FIG. 1. Circuit for the DJFQ as described in the text. Josepshon junctions 1 and 2 have Josepshon energy E_J and capacitance C, and junction 3 has Josepshon energy and capacitance α times smaller. The arrows indicate the sign convention for defining the gauge-invariant phase differences. The circuit encloses a magnetic flux $\Phi=f\Phi_0$.

dynamical variables: φ_1,φ_2. The circuits that are used for the DJFQ have two of the junctions with the same coupling energy, $E_{J,1}=E_{J,2}=E_J$, and capacitance, $C_1=C_2=C$, while the third junction has smaller coupling $E_{J,3}=\alpha E_J$ and capacitance $C_3=\alpha C$, with $0.5<\alpha<1$. In terms of the two-dimensional coordinate $\vec{\varphi}=(\varphi_1,\varphi_2)$, the Hamiltonian of the DJFQ is[2]

$$\mathcal{H}=\frac{-\eta^2}{2}\nabla_\varphi^T\mathbf{m}^{-1}\nabla_\varphi+V(\vec{\varphi}), \tag{1}$$

where we have normalized $\mathcal{H}$ by the Josephson coupling energy E_J, and $\eta^2=8E_C/E_J$, with $E_C=e^2/2C$. The kinetic term of the Hamiltonian corresponds to the electrostatic energy of the system, where the momentum operator is $\hat{\vec{P}}=-i\hbar\nabla_\varphi$, with $\nabla_\varphi=(\frac{\partial}{\partial\varphi_1},\frac{\partial}{l\varphi_2})$, and the "mass" tensor is given by the matrix $\mathbf{m}$,

$$\mathbf{m}=\begin{pmatrix}1+\alpha & -\alpha\\ -\alpha & 1+\alpha\end{pmatrix}.$$

The potential term of the Hamiltonian corresponds to the Josephson energy of the junctions and is given by

$$V(\vec{\varphi})=2+\alpha-\cos\varphi_1-\cos\varphi_2-\alpha\cos(2\pi f+\varphi_1-\varphi_2). \tag{2}$$

Typical flux qubit experiments have values of α in the range 0.6–0.9 and η in the range 0.1–0.6.[6–8,15]

In quantum computation implementations[2,6,7] the Josephson flux qubit is operated at (static) magnetic fields near the half-flux quantum, $f=1/2+\delta f$, with $\delta f\ll 1$. For $\alpha\geq 1/2$, the potential of Eq. (2) has the shape of a double well with two minima (within the domain $-\pi<\varphi_1<\pi$, $-\pi<\varphi_2<\pi$). After a change in variables one can define the transverse phase $\varphi_t=(\varphi_1+\varphi_2)/2$ and the longitudinal phase $\varphi_l=(\varphi_1-\varphi_2)/2$, obtaining

$$V(\vec{\varphi})=2+\alpha-2\cos\varphi_t\cos\varphi_l-\alpha\cos(2\pi f+2\varphi_l). \tag{3}$$

The two minima are along the longitudinal direction φ_l, at $(\varphi_l,\varphi_t)=(\pm\varphi^*,0)$ separated by a maximum at $(\varphi_l,\varphi_t)=(0,0)$. Each minima corresponds to macroscopic persistent currents of opposite sign. Experimental measurements are sensitive to the sign of the persistent current[6] and therefore

they detect the probability of being on one side or the other of the double-well potential. For $\delta f>0$ ($\delta f<0$) a ground state $|-\rangle$ ($|+\rangle$) with negative (positive) persistent current is favored with energy $\epsilon_{\pm}\propto\pm\delta f$. At $\delta f=0$ the two minima have the same energy and the two lowest energy eigenstates ($|\Psi_0\rangle$ and $|\Psi_1\rangle$) are symmetric and antisymmetric superpositions of the two states ($|-\rangle$ and $|+\rangle$) corresponding to the macroscopic persistent currents. To describe the dynamics of the device as a quantum bit, a two-level truncation of the Hilbert space is performed.[2] In the subspace expanded by $|\Psi_0\rangle$ and $|\Psi_1\rangle$, the Hamiltonian of Eq. (1) is reduced to

$$\mathcal{H}_{\mathrm{TLS}}=-\frac{\epsilon}{2}\hat{\sigma}_z-\frac{\Delta}{2}\hat{\sigma}_x, \tag{4}$$

where $\mathcal{H}_{\mathrm{TLS}}$ is written in the basis defined by $|+\rangle=(|\Psi_0\rangle+|\Psi_1\rangle)/\sqrt{2}$ and $|-\rangle=(|\Psi_0\rangle-|\Psi_1\rangle)/\sqrt{2}$. Here $\Delta=E_1-E_0$ is the two-level splitting at $\delta f=0$, and $\epsilon=4\pi\alpha E_J S_{01}\delta f$ (for $\delta f\ll 1$), with $S_{01}=-\langle\Psi_0|\sin(2\varphi_l)|\Psi_1\rangle=-\langle+|\sin(2\varphi_l)|+\rangle$. (For typical values of α and η, one has $S_{01}\sim 0.8-0.9$). Most experiments control the system varying the magnetic field detuning δf. The magnitude of the gap Δ depends exponentially on α and η. Recently it has been shown experimentally that it is possible to manipulate the value of Δ by controlling α, replacing the third junction by an additional SQUID loop.[24,25]

Landau-Zener-Stückelberg (LZS) interferometry is performed by applying an harmonic field on top of the static field such that $f\to f(t)$ with

$$f(t)=f_0+f_p\sin(\omega t). \tag{5}$$

Hence Eq. (4) acquires an explicit dependence on time through $\epsilon\to\epsilon(t)=\epsilon_0+A\sin(\omega t)$ with $\epsilon_0=4\pi\alpha E_J S_{01}\delta f$, $\delta f=f_0-1/2$ and $A\equiv 4\pi\alpha E_J S_{01} f_p$. The initial state corresponds to prepare the system in the ground state $|0,f_0\rangle$ for the static field f_0.

For values of $|\delta f|\ll 1$ and small driving amplitudes $f_p\ll 1$, the DJFQ is adequately described as a TLS, whose time evolution under an harmonic drive does not have, in general, an exact solution. Thus the dynamics is usually approximated[17,26] by free evolutions of the basis states mediated by nonadiabatic LZ transitions,[27] with probability $P_{\mathrm{LZ}}=\exp(-2\pi\delta)$ with $\delta=\Delta^2/f_p\omega$. In the last case, explicit expressions for the occupation probability have been obtained in the fast (slow) driving regime,[17,26] $\delta\ll(\gg)1$.

Here we will consider the case of nearly fast driving, which corresponds to the series of experiments on amplitude spectroscopy performed in Ref. 15. For $f_0\lesssim 1/2$, the system is started in the ground state $|0,f_0\rangle\approx|+\rangle$, which has a positive persistent current. In this type of experiments, one asks for the probability of switching to a state of negative persistent current: $P_{|+\rangle\to|-\rangle}=P_-(t)$ during the time the harmonic pulse is applied. For the TLS in the fast driving regime, the occupation probability P_- is approximately given as[17,26]

$$P_-^{TFD}(t)=\sum_n\frac{\Gamma_n^2}{2\Omega_n^2}\{[1-\cos(\Omega_n t)]\},$$

$$\Gamma_n=\Delta J_n(A/\omega),$$

$$\Omega_n=\sqrt{(n\omega-\epsilon_0)^2+\Gamma_n^2}, \tag{6}$$

being $J_n(z)$ the order n Bessel function of the first kind. The resonance condition $\epsilon_0=n\omega$ is attained when the total phase accumulated over a single period of the driving, $\Theta=2\pi\epsilon_0/\omega$, satisfies $\Theta=2\pi n$ for a given integer n.[13,17] Under resonance, the occupation probability $P_-^{TFD}(t)\to 1/2[1-\cos(\Omega_n t)]$ with $\Omega_n=\Delta J_n(A/\omega)$. Notice that Ω_n depends on the driving amplitude f_p through A.

Besides the time dependence, the average occupation probability is the key quantity for the spectroscopic analysis performed in recent experiments.[13,15] In the case of a TLS in the fast driving regime, the average occupation probability obtained from Eq. (6) is a sum of Lorentzian-shape n-photon resonances[13]

$$\overline{P_-^{TFD}}=\frac{1}{2}\sum_n\frac{\Gamma_n^2}{(n\omega-\epsilon_0)^2+\Gamma_n^2}. \tag{7}$$

Thus as ϵ_0 (or δf) is changed, different n resonances are explored. In addition the Bessel function entering in Γ_n gives a quasiperiodic character to the patterns of resonances as the amplitude f_p is varied keeping the frequency ω fixed.

The analysis of the positions of the resonances as a function of f_p and δf was the route followed in Refs. 13 and 15 in an effort to obtain the parameters characterizing the different avoided crossings of the flux qubit.

III. AMPLITUDE SPECTROSCOPY FOR COHERENT SYSTEMS

A. Direct numerical calculation

In this section we will focus on the study of the quantum dynamics of the DJFQ driven by the time-dependent flux $f(t)$ given in Eq. (5) for f_0 near 1/2 and varying the amplitude f_p of the harmonic drive.

In the absence of driving, i.e., for $f_p=0$, the eigenvectors $\Psi_n(\vec{\varphi})$ and eigenenergies E_n are obtained by solving,

$$\left[-\frac{\eta^2}{2}\nabla_\varphi^T\mathbf{m}^{-1}\nabla_\varphi+V(\vec{\varphi})\right]\Psi_n(\vec{\varphi})=E_n\Psi_n(\vec{\varphi}). \tag{8}$$

In Fig. 2 we plot the seven lower energy levels as a function of flux detuning f_0, obtained by numerical diagonalization of Eq. (8) using a discretization grid of $\Delta\varphi=2\pi/M$ and 2π-periodic boundary conditions on $\vec{\varphi}=(\varphi_1,\varphi_2)$. In this case we set $\eta=0.25$ and $\alpha=0.8$, close to the experimental values employed in flux qubits experiments.[2,15] The energy spectrum is rather sensitive to the values of η and α, and, in particular, for the selected values, the energy landscape is quite involved, presenting many avoided crossings Δ_{ij} in the range $0.45<f_0<0.55$. The slope of the energy levels dE_n/df_0 is proportional to the average current in the loop. Therefore an eigenstate with positive or negative slope corresponds to a wave function mostly weighted in one side or the other of the double well. A gap Δ_{ij} opens at the avoided crossings of energy levels of opposite slope. We label the gaps Δ_{ij} as the avoided crossing of the ith level of positive slope with the jth level of negative slope, see Fig. 2. (This convention is different from the one used in Ref. 15 where a

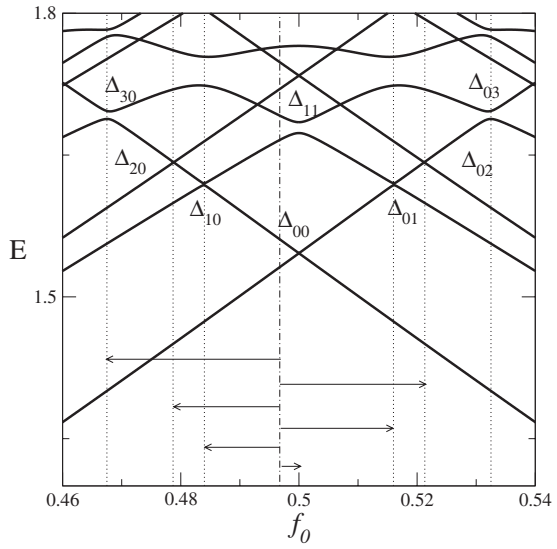

FIG. 2. Lowest seven energy levels of the DJFQ as a function of flux f_0 for $\eta=0.25$ and $\alpha=0.80$. Arrows indicate the position of the avoided level crossings Δ_{ij} measured from $f_0=0.497$ (indicated by the vertical dot-dashed line). Calculations were done using $M=256$ (see the text for details). Energy is measured in units of E_J and flux in units of Φ_0.

distinction among longitudinal and transverse modes is made in the labeling of the gaps.)

It is evident from the energy-level diagram of Fig. 2 that the description of the time evolution of the DJFQ in terms of a TLS is valid only for a very small range of amplitudes f_p.

In the presence of a finite driving amplitude f_p, our first approach to the problem is to solve numerically the time-dependent Schrödinger equation (we have normalized time by $t_J=\hbar/E_J$),

$$i\frac{\partial\Psi(\vec{\varphi},t)}{\partial t}=\mathcal{H}\Psi(\vec{\varphi},t). \tag{9}$$

We integrate numerically Eq. (9) with a second-order split-operator algorithm,[28] using a discretization grid of $\Delta\varphi=2\pi/M$ and $\Delta t=0.1t_J$. We use 2π-periodic boundary conditions on $\vec{\varphi}=(\varphi_1,\varphi_2)$. The system is started in the ground state $|0,f_0\rangle$ for a given static field f_0, obtained from the numerical solution of Eq. (8). Experimentally, what is measured is the probability of being in a given state of positive, P_+, or negative, P_-, persistent current, which can be obtained as

$$P_+(t)\equiv 1-P_-(t)=\int_{\pi>\varphi_l>0}|\Psi(\varphi_1,\varphi_2,t)|^2d\varphi_1d\varphi_2, \tag{10}$$

where the integration is on one side of the double-well potential defined by $\varphi_l>0$ (i.e., $-\pi\leq\varphi_1\leq\pi$ and $\varphi_2\leq\varphi_1$). The quantity measured experimentally is the long-time occupation probability, which is equivalent to the time-averaged probability in the stationary state. In Fig. 3 we plot the time-averaged probability $\bar{P}_-=1-\bar{P}_+$ as a function of the static flux f_0 and the amplitude f_p of the harmonic excitation. The average is performed over several periods of the harmonic

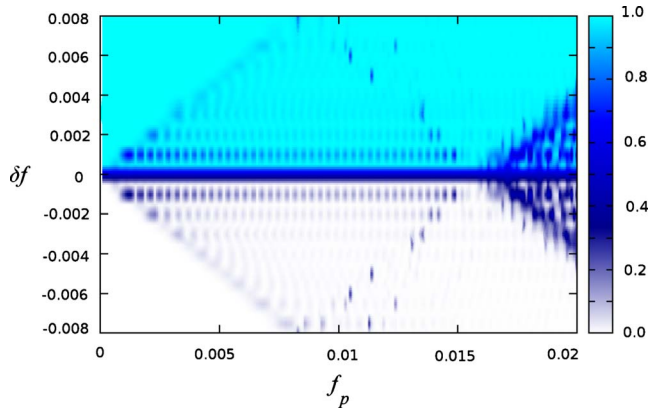

FIG. 3. (Color online) Large-amplitude spectroscopic diamonds obtained for the Josephson flux qubit with $\eta=0.25$ and $\alpha=0.8$. The intensity of $\bar{P}_-$ is plotted as a function of flux detuning δf and rf amplitude f_p. The system is driven at a frequency $\omega=0.001$ (in units of $E_J/\hbar$). Numerical calculations were done by direct numerical integration using $M=128$ and $\Delta t=0.1t_J$. Data points correspond to a grid of $\Delta f_0=1\times10^{-3}$ and $\Delta f_p=1\times10^{-4}$.

drive (typically ~20–100 periods, until convergence of the average). The plot is obtained by calculating points with a grid of $\Delta f_0=1\times10^{-3}$ and $\Delta f_p=1\times10^{-4}$. A pattern of "spectroscopic diamonds" is observed, similar to the one obtained in the experiments, which can be related to the energy-level spectrum of Fig. 2 as follows. At a fixed flux detuning $\delta f=f_0-1/2$, the first diamond, D1, starts when the Δ_{00} avoided crossing is reached, at $f_p=f_{1s}=f_{00}-f_0=-\delta f$, with $f_{00}=1/2$ the location of Δ_{00}. The first diamond ends when the Δ_{10} crossing is reached at $f_p=f_{1e}=f_0-f_{10}$ with f_{10} the location of Δ_{10}. Then the second diamond, D2, starts when the Δ_{01} avoided crossing is reached, at $f_p=f_{2s}=f_{01}-f_0$, with f_{01} the location of Δ_{01}, etc. The spectroscopic diamonds of Fig. 3 have much less contrast than in the experiments of Ref. 15 in which the contrast is due to fast intrawell relaxation. This induces population inversion, reducing the population in the sectors between the diamonds (i.e., for example, between D1 and D2). In DJFQs with less relaxation effects, the picture should be closer to the one shown in Fig. 3. Within the first diamond a regular pattern of resonances can be qualitatively observed in Fig. 3. However to accurately describe all the resonances of D1, as well as the complex structure of D2, a finer grid sampling $\Delta f_0,\Delta f_p$ is needed. Furthermore, simulations at high f_p, in the region of the second diamond and above (where the dynamics has more weight in higher energy levels), need a better discretization of the Schrödinger equation and averaging of the population for larger times. Therefore a finer description of the structure of diamonds needs large time-consuming simulations of the full time-dependent Schrödinger equation. Instead, in the following we will employ an approach based on the Floquet formalism, more adequate for time periodic Hamiltonians.

B. Floquet formulation

For a finite driving $f(t)$, we write $\mathcal{H}=\mathcal{H}_0+\delta V(\vec{\varphi},t)$ with $\mathcal{H}_0$ corresponding to Eq. (1) with $f=f_0$ (i.e., the time-independent part of the Hamiltonian) and

$$\delta V(\vec{\varphi},t) = \alpha E_J \sin[2\pi f_{\rm ac}(t)]\sin(2\pi f_0 + \varphi_1 - \varphi_2) + 2\alpha E_J \sin^2[\pi f_{\rm ac}(t)]\cos(2\pi f_0 + \varphi_1 - \varphi_2), \tag{11}$$

where $f_{\rm ac}(t)=f_p \sin(\omega t)$. The potential defined in Eq. (11) is periodic in time with period $T=2\pi/\omega$. Thus, according to the Floquet theorem,[20] the time-dependent Schrödinger equation, Eq. (9), has a solution that can be written as

$$\Psi_\alpha(t) = e^{-i\varepsilon_\alpha t}\Phi_\alpha(t), \tag{12}$$

where $\Phi_\alpha(t)=\Phi_\alpha(t+T)$ and ε_α is known as the quasienergy or Floquet eigenvalue.

Substituting expression (12) into Eq. (9) we obtain an eigenvalue equation for the quasienergies,

$$\hat{H}_F(t)\Phi_\alpha(t) = \varepsilon_\alpha \Phi_\alpha(t), \tag{13}$$

where the Floquet Hamiltonian is defined as

$$\hat{H}_F(t) = \mathcal{H}(t) - i\frac{\partial}{\partial t}. \tag{14}$$

Since the function $\Phi_\alpha(t)$ is periodic in time it can be expanded in a Fourier series. We introduce the standard Floquet nomenclature[22] and define $|n,k\rangle=|n\rangle\otimes|k\rangle$, where n is an index that labels the eigenstates of H_0 and k is a Fourier index. Then

$$\langle n|\Phi_\alpha(t)\rangle = \sum_{k=-\infty}^{\infty} \langle n,k|\phi_\alpha\rangle e^{-ik\omega t}, \tag{15}$$

where $\langle n,k|\phi_\alpha\rangle$ is a Fourier amplitude. From Eqs. (13)–(15) it is straightforward to write

$$\varepsilon_\alpha\langle n,q|\phi_\alpha\rangle = \sum_m \sum_k \langle n,q|\hat{H}_F|m,k\rangle\langle m,k|\phi_\alpha\rangle, \tag{16}$$

where $\hat{H}_F$ is the Floquet Hamiltonian previously defined whose matrix elements are given by

$$\langle n,q|\hat{H}_F|m,k\rangle = (E_n + q\omega)\delta_{m,n}\delta_{k,q} + \frac{\omega}{2\pi}\int_0^{2\pi/\omega} \langle n|\delta V(\vec{\varphi},t)|m\rangle e^{-i(q-k)\omega t}dt. \tag{17}$$

Then the time-dependent problem is reduced to solve the eigenvalue equation, Eq. (16).

We need to calculate the matrix elements of the Floquet Hamiltonian defined in Eq. (17). As it was mentioned before, the first term in this equation is obtained by numerical diagonalization of Eq. (8), using a discretization grid of $\Delta\varphi=2\pi/M$ and 2π-periodic boundary conditions on $\vec{\varphi}=(\varphi_1,\varphi_2)$. The second term in Eq. (17) is written as

$$V^l_{nm} = \frac{\omega}{2\pi}\int_0^{2\pi/\omega} \langle n|\delta V(\vec{\varphi},t)|m\rangle e^{-il\omega t}dt, \tag{18}$$

where $\delta V(t)$ was defined in Eq. (11) and $l=q-k$ is an integer. The integration is straightforward and we obtain

$$V^l_{nm} = \alpha E_J \times \begin{cases} \mathcal{C}_{nm}[\delta_{l0} - J_l(2\pi f_p)] & \text{for } l \text{ even} \\ i\mathcal{S}_{nm}J_l(2\pi f_p) & \text{for } l \text{ odd}, \end{cases} \tag{19}$$

where $\mathcal{S}_{nm}=\langle n|\sin(2\pi f_0+\varphi_1-\varphi_2)|m\rangle$, $\mathcal{C}_{nm}=\langle n|\cos(2\pi f_0+\varphi_1-\varphi_2)|m\rangle$, and $J_l(x)$ is the Bessel function of first kind of order l.

Then we have all the ingredients to construct the Floquet matrix,

$$\langle n,q|\hat{H}_F|m,k\rangle = (E_n + q\omega)\delta_{m,n}\delta_{k,q} + V^{q-k}_{nm}, \tag{20}$$

where q and k range over all integers form $-\infty$ to ∞. In order to solve the problem numerically we must truncate the Floquet matrix, Eq. (20). The truncated matrix is of dimension $N_d=(2K+1)N_l$, where K is defined by the maximum value of the Fourier index and N_l by the number of levels considered in the diagonalization of Eq. (8).

Floquet eigenstates and quasienergies contain all the information to construct the large-amplitude spectroscopic diamonds. Following the experiments, we take as initial state the ground state of $\mathcal{H}_0$ for a given value of flux detuning f_0 that here for simplicity, we denote $|0\rangle$. The initial state is prepared at a time t_0 and then at a time t the evolved solution $|\Psi(t,t_0)\rangle$ can be expanded in the basis of eigenstates of $\mathcal{H}_0$ as

$$\Psi(\varphi_1,\varphi_2,t,t_0) = \sum_n c_n(t,t_0)\chi_n(\varphi_1,\varphi_2), \tag{21}$$

where $\chi_n(\varphi_1,\varphi_2)=\langle\varphi_1,\varphi_2|n\rangle$ is the wave-function representation of eigenket $|n\rangle$ in terms of the variables (φ_1,φ_2).

Using the Fourier amplitudes of the Floquet eigenstates $\langle n,k|\phi_\alpha\rangle$, and their corresponding eigenenergies ε_α, one obtains the coefficients[22]

$$c_n(t,t_0) = \sum_k \sum_\beta \langle n,k|\phi_\beta\rangle\langle\phi_\beta|0,0\rangle e^{-i\varepsilon_\beta(t-t_0)}e^{i\omega kt}, \tag{22}$$

which are the probability amplitudes that the system initially in the ground state at time t_0 evolves to a state $|n\rangle$ by time t according to the time-periodic Hamiltonian. This equation can be interpreted as the amplitude probability that the system initially in the Floquet state $|0,0\rangle$ at time t_0 evolve to the Floquet state $|n,k\rangle$ by time t according to the time-independent Floquet Hamiltonian, summed over k with weighting factors $\exp(i\omega kt)$.

We can now calculate the time dependence of the probability P_+ (or $P_-=1-P_+$) of a measurement of a positive (negative) state of persistent current, replacing Eqs. (21) and (22) into Eq. (10), and obtaining

$$P_+(t,t_0) = \sum_n \sum_m \lambda_{nm}(t,t_0)p_{nm}, \tag{23}$$

where the coefficients

$$p_{nm} = \int_{\mathcal{W}} \chi_n(\varphi_1,\varphi_2)\chi^*_m(\varphi_1,\varphi_2)d\varphi_1 d\varphi_2 \tag{24}$$

are evaluated by numerical integration using the eigenstates of Eq. (8) and $\mathcal{W}$ is the triangular sector of the two-dimensional space defined by $\varphi_l>0$ (i.e., $-\pi\le\varphi_1\le\pi$ and $\varphi_2\le\varphi_1$). The time-dependent coefficients $\lambda_{nm}(t,t_0)=c_n(t,t_0)c^*_m(t,t_0)$ are calculated as

$$\lambda_{nm}(t,t_0) = \sum_{k,l}\sum_{\beta,\gamma}\langle n,k|\phi_\beta\rangle\langle\phi_\beta|0,0\rangle\langle 0,0|\phi_\gamma\rangle \times\langle\phi_\gamma|m,l\rangle e^{-i(\varepsilon_\gamma-\varepsilon_\beta)(t-t_0)}e^{i\omega(k-l)t}. \quad (25)$$

We can calculate now the time average of $P_+(t)$. To this end, we average $\lambda_{nm}(t,t_0)$ over many periods considering that for long times $\overline{e^{i[\omega(k-l)+\varepsilon_\gamma-\varepsilon_\beta]t}}=\delta_{\omega(k-l),\varepsilon_\beta-\varepsilon_\gamma}$. Using the periodic properties of the quasienergies and eigenvectors of the Floquet Hamiltonian,[22] we get

$$\bar{\lambda}_{nm}(t_0) = \sum_{k,l}\sum_{\beta}\langle n,k|\phi_\beta\rangle\langle\phi_\beta|0,0\rangle\langle 0,k-l|\phi_\beta\rangle \times\langle\phi_\beta|m,k\rangle e^{i\omega(k-l)t_0}. \quad (26)$$

In experiments the initial time, or equivalently the initial phase of the field seen by the system in repeated realizations of the measurement, is not well defined. Then, the quantity of interest is the transition probability averaged over initial times,[22] in which case $\overline{e^{i\omega(k-l)t_0}}=\delta_{k,l}$. Finally, we obtain

$$\bar{P}_+ = \sum_{n,m} p_{nm}\Lambda_{nm}, \quad (27)$$

where

$$\Lambda_{nm} = \sum_{\beta}\sum_{k}\langle n,k|\phi_\beta\rangle\langle\phi_\beta|0,0\rangle\langle 0,0|\phi_\beta\rangle\langle\phi_\beta|m,k\rangle.$$

Thus once equipped with the Floquet quasienergies and eigenstates one can either compute the time-dependent occupation probability, Eq. (23), or the time-averaged probability, Eq. (27), which is indeed an exact average.

To summarize, we follow this procedure: (i) we take the parameters η and α from the experimental device. (Here we use $\eta=0.25$ and $\alpha=0.8$.) (ii) For each value of the magnetic flux f_0 we solve numerically the eigenvalue Eq. (8) obtaining the eigenstates $\chi_n(\varphi_1,\varphi_2)$ and eigenvalues E_n, with a discretization $\Delta\varphi=2\pi/M$ ($M=256-1024$). (iii) We evaluate the Floquet matrix elements of Eq. (19) and the coefficients p_{nm} of Eq. (24). (iv) We solve numerically the Floquet eigenvalue equation, Eqs. (16) and (20) obtaining the Floquet eigenvalues ε_α and the components $\langle n,q|\phi_\alpha\rangle$ of the corresponding eigenvectors. A truncation of the matrix is performed: we consider N_l energy levels (results for different N_l will be shown) and we consider $2K+1$ Fourier components in $-K<k<K$. Large K is chosen until convergence of the quantities of interests. ($K\sim 150-400$). (v) The time-dependent occupation probability, Eq. (23), for $t_0=0$, or the time-averaged probability, Eq. (27), are then evaluated, with the sums over energy levels between 0 and N_l-1, the sums over k components between $-K$ and K, and the sums over Floquet states between 1 and $N_d=N_l(2K+1)$.

1. Time-dependent occupation probabilities

We start analyzing the explicit time dependence of the probability $P_-(\tau)$ after a driving of duration τ is applied. To this end, we evaluate numerically Eq. (23) for $t_0=0$. Different initial states shall correspond to prepare the system in the ground state $|n=0;f_0\rangle$ for different $f_0\lesssim 0.5$.

For values of $\delta f=f_0-1/2$ and (rather small) driving amplitudes f_p, such that Δ_{00} is the only relevant avoided crossing (see Fig. 2), the DJFQ can be described as a TLS. In Fig. 4 we plot $P_-(\tau)=1-P_+(\tau)$ as a function of time $\tau=\omega t/2\pi$ in units of the pulse period, for small f_p. The numerical calculations were performed with the Floquet formalism, employing in Eq. (23) the lowest six energy levels ($N_l=6$) and $K=150-250$. For this case, we find that calculations with $N_l=2$ levels overlap almost exactly with the $N_l=6$ calculations, and can not be distinguished in the plot, since the TLS approximation is correct for small f_p, as expected. In panel (a) we consider the case with frequency $\omega=0.001$ and with $\delta f=-0.11\times10^{-3}$ such that it corresponds to the fast driving TLS $n=1$ resonance, $\epsilon_0=\omega$. For the selected amplitude, $f_p=0.25\times10^{-3}$, the behavior of $P_-(\tau)$ is on the global scale rather well described by the fast driving approximation for a TLS given by Eq. (6). The numerically obtained frequency is very close to $\Omega_1\sim\Gamma_1=1.87\times10^{-4}$, in agreement with the on-resonance relation written in Eq. (6). However, $P_-(\tau)$ exhibits sudden jumps mediated by additional oscillations with n local maxima on time scales $\sim\pi/\omega$. These oscillations reflect the quantum-mechanical interference between consecutive passages through the avoided crossing Δ_{00}. This behavior is not captured by the fast driving TLS expression, Eq. (6), plotted for comparison by the red dashed line. In the present case $\delta=\Delta_{00}^2/\omega f_p\simeq 0.5$ and then, the interference effects are important. In panel (b) we consider for the same

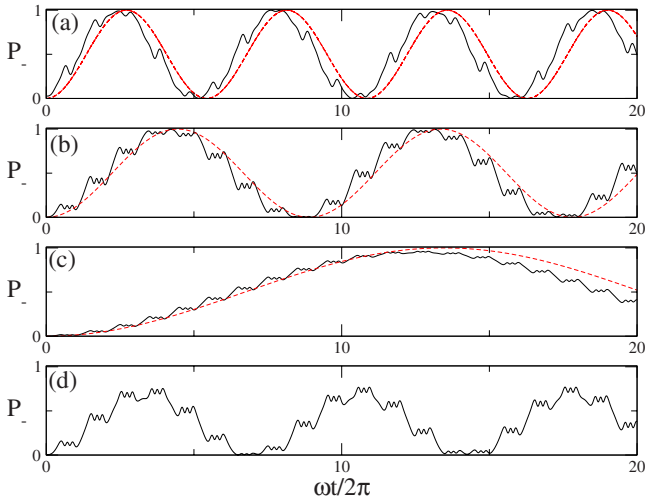

FIG. 4. (Color online) P_- as a function of time $\tau=\omega t/2\pi$ for $\eta=0.25$ and $\alpha=0.8$. (a) $\epsilon_0=\omega$, for $\omega=0.001$, $\delta f=-0.11\times10^{-3}$, and $f_p=0.24\times10^{-3}$ (black solid line). The fast driving TLS Eq. (6) for $n=1$ with $\Omega_1=\Delta_{00}J_1(4\pi S_{01}f_p/\omega)=1.87\times10^{-4}$ is plotted for comparison (red dashed line). (b) $\epsilon_0=3\omega$, for $\omega=0.001$, $\delta f=-0.33\times10^{-3}$, and $f_p=0.35\times10^{-3}$ (black solid line). The fast driving TLS Eq. (6) for $n=3$ with $\Omega_3=\Delta_{00}J_3(4\pi S_{01}f_p/\omega)=1.14\times10^{-4}$ is plotted for comparison (red dashed line). (c) $\epsilon_0=3\omega$, for a higher frequency $\omega=0.003$, $\delta f=-0.99\times10^{-3}$, and $f_p=1.05\times10^{-3}$ (black solid line). Notice that the oscillations on time scales $\sim\pi/\omega$ are smaller for $\omega=0.003$, as described in the text. The fast driving TLS Eq. (6) for $n=3$ is plotted for comparison (red dashed line). (d) Out of ($n=3$) resonance, for $\omega=0.001$, $\delta f=-0.32\times10^{-3}$, and $f_p=0.35\times10^{-3}$ (black solid line). Notice that the oscillations on time scales $\sim\pi/\omega$ persist. Numerical calculations were done with $N_l=6$ levels, $K=180$ and $M=1024$. Calculations with $N_l=2$ levels overlap almost exactly with the $N_l=6$ calculations in this case.

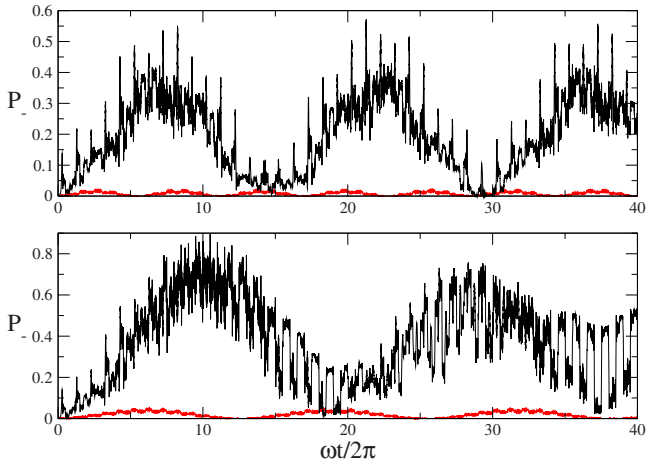

FIG. 5. (Color online) P_- as a function of time $\tau=\omega t/2\pi$ for $\eta=0.25$ and $\alpha=0.8$. The flux qubit is driven at a strong amplitude with $f_p=16\times10^{-3}$. (a) Resonance condition for the TLS in the fast driving regime: $\epsilon_0=3\omega$, for $\omega=0.001$ and $\delta f=-0.33\times10^{-3}$. (b) $\epsilon_0\neq n\omega$, for $\omega=0.001$ and $\delta f=-0.32\times10^{-3}$. Numerical calculations were done with $N_l=6$ levels, $K=300$ and $M=1024$. Calculations with $N_l=2$ levels are plotted for comparison (lower curve, red line).

frequency as in (a), the case of $\delta f=-0.33\times10^{-3}$ to select the fast driving TLS $n=3$ resonance ($\epsilon_0=3\omega$). For a small amplitude $f_p=0.35\times10^{-3}$, the qualitative description given for panel (a) holds. For the driving parameters used in panel (b) we have an adiabaticity parameter $\delta\simeq0.25$. In this case the oscillations on time scales $\sim\pi/\omega$, exhibit $n=3$ local maxima. In panel (c) we also consider the case of the $n=3$ resonance but at a higher frequency, $\omega=0.003$, for which $\delta\simeq0.03$. In this case the fast driving approximation is more adequate, the local oscillations on time scales $\sim\pi/\omega$ are washed out, improving the agreement with the fast driving TLS expression, Eq. (6). This can be understood taking into account that the (adiabatic) Landau-Zener transition probability[27] at a single avoided crossing diminishes as the frequency ω increases. In Fig. 4(d) $P_-(\tau)$ is plotted for $\delta f=-0.32\times10^{-3}$ and $\omega=0.001$, a value which is out but close to the $n=3$ resonance. We employ the same amplitude $f_p=0.35\times10^{-3}$ as in Fig. 4(b). Notice that in this case is $\max[P_-(\tau)]<1$, as expected in the off-resonance situation, but the short-time scale oscillations on time scales $\sim\pi/\omega$ persist.

In Fig. 5 we show that for a larger amplitude $f_p=16\times10^{-3}$ the TLS approach breaks down. For this amplitude, the system is driven close to the avoided crossing Δ_{01} (see Fig. 2). In panel (a) we show the case where $\epsilon_0=3\omega$ is satisfied while in panel (b) we show the case out of the $\epsilon_0=3\omega$ condition. As expected, the magnitude of $\max[P_-(\tau)]$ in this case is completely unrelated with the resonance conditions observed at smaller f_p. We also compare the results obtained considering up to $N_l=6$ levels when evaluating Eq. (23) with the case with only $N_l=2$ levels. As it is evident in the plots, for this large amplitude more than two levels are needed to describe the behavior of $P_-(\tau)$, since most of the population is at the higher energy eigenstates.

2. Average occupation probabilities

Besides the time dependence, the average occupation probability, Eq. (27), is the key quantity for the spectroscopic analysis performed in recent experiments.[13,15] We analyze the patterns of $\bar{P}_-$ in the $(f_p,\delta f)$ space. As we shall show below, as the amplitude f_p is increased, $\bar{P}_-$ will exhibit a richer and more involved structure.

Regarding the parameters employed in the numerical calculations, for small driving amplitude f_p and flux detuning $f_0\simeq0.5$, the discretization grid needed to compute the eigenstates $|n;f_0\rangle$ can be constructed with quite small values of $M\sim128$.[11] However, in the strong driving regime, we need to use $M=256-1024$. In addition, we employ $K\sim150-400$ to attain convergence in the values of $\bar{P}_-$. As we already mentioned N_l is mainly determined by f_p. All the calculations, otherwise specified, have been performed with the lowest six levels.

In Fig. 6(a) we show the contour plot of $\bar{P}_-$ as a function of $(f_p,\delta f)$ for $\delta f<0$ and $\omega=0.001$. The range of values of f_p and δf has been selected to explore the region of the energy spectrum of Fig. 2 containing the avoided crossings Δ_{00}, Δ_{10}, Δ_{11}, and Δ_{20}. The plot is obtained by calculating points with a grid of $\Delta f_0=2\times10^{-5}$ and $\Delta f_p=3\times10^{-5}$. A clear pattern of maxima and minima forming a half diamondlike structure can be observed in Fig. 6(a). For the sake of clarity we have drawn lines indicating the boundaries of the first (half) diamond D1 and the beginning of the second one D2. For $\delta f>0$ the diamond pattern is completed with $1-\bar{P}_-$. The qualitative agreement with the diamond structure observed in Ref. 15 is evident. However, in this coherent regime the spectroscopic diamonds have much less contrast than in the experiments of Ref. 15.

In Fig. 6(b) we show a similar contour plot of $\bar{P}_-$ for a higher frequency $\omega=0.002$. A very similar pattern of maxima and minima forming a half diamondlike structure can be observed in Fig. 6(b). For this larger driving frequency the distance between resonances is increased, as it is expected from Eq. (6). It is important to remark that when we increase the driving frequency and thus the sweep rate, we lose resolution in the obtained spectroscopic diamonds as it can be checked by inspection of Figs. 6(a) and 6(b).

Emulating the experimental protocol, in the following we analyze the structure of the diamonds in order to extract spectroscopic information, focusing on a fixed frequency, $\omega=0.001$. We start by considering a particular static flux detuning $f_0\simeq0.49691$, i.e., $\delta f\simeq-0.00309$ [black dot in Fig. 6(a) and vertical dashed-dotted line in Fig. 2] that satisfies for $\omega=0.001$ the fast driving TLS $n=28$ resonance condition, $\epsilon_0=28\omega$. The initial ground state is $|0;0.49691\rangle$ and thus for $f_p=0$ is $\bar{P}_-=0$. As the driving amplitude is increased, the net transfer of population over many driving periods will translate in a finite value of $\bar{P}_-$. Along the horizontal line defined at $\delta f\simeq-0.00309$ in Fig. 6(a), the first diamond D1 starts at $f_p^D=0.003$ (D labels the parameters extracted from the diamonds). From Fig. 2 one can check that this value is roughly the threshold amplitude needed to reach the first avoided crossing Δ_{00} for the considered value of $f_0=0.49691$. For

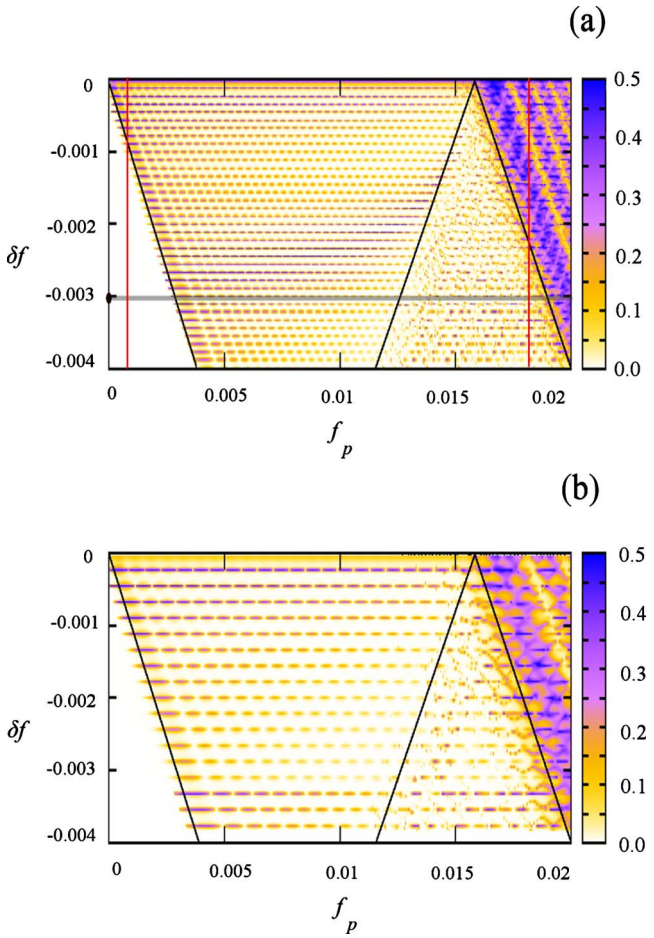

FIG. 6. (Color online) Large-amplitude spectroscopic (half) diamonds obtained for the Josephson flux qubit with $\eta=0.25$ and $\alpha=0.8$. The intensity of $\bar{P}_-$ is plotted as a function of flux detuning δf and rf amplitude f_p. (a) The system is driven at a frequency $\omega=0.001$. Calculations were done using $N_l=6$ (six levels), $150\leq K\leq 300$ and $M=1024$. The black solid lines indicate the edges of the first diamond D1 and the beginning of the second one D2. The black dot indicates a particular value of flux detuning $\delta f\simeq -0.003$ for $f_p=0$. See text for a detailed analysis. (b) The flux qubit is driven at a frequency $\omega=0.002$. Calculations were done using $N_l=6$, $150\leq K\leq 250$ and $M=1024$. Data points correspond to a fine grid of $\Delta f_0=2\times 10^{-5}$ and $\Delta f_p=3\times 10^{-5}$.

$f_p>0.003$ the multiple passages through the avoided crossing Δ_{00} are reflected in the observed interference pattern that, up to $f_p\sim 0.01$, it is rather well described by the quasiperiodic behavior of the Bessel function $J_{n=28}(4\pi\alpha E_J S_{01} f_p/\omega)$ entering in the definition of $\Gamma_{n=28}$ in Eq. (7). If the driving amplitude f_p is further increased the interference patterns persist, but the positions of the maxima and minima do not follow the Bessel function dependence, as the description of the resonances in terms of the fast driving TLS formula is not accurate for these amplitudes. A detailed evidence of this behavior is shown in Fig. 7(a) where we plot a cut of $\bar{P}_-$ along the horizontal line $\delta f=-0.00309$ depicted in Fig. 6(a), corresponding to the condition $\varepsilon_0=28\omega$ ($n=28$ resonance condition for the TLS in the fast driving regime), together with the same quantity computed keeping only the lowest

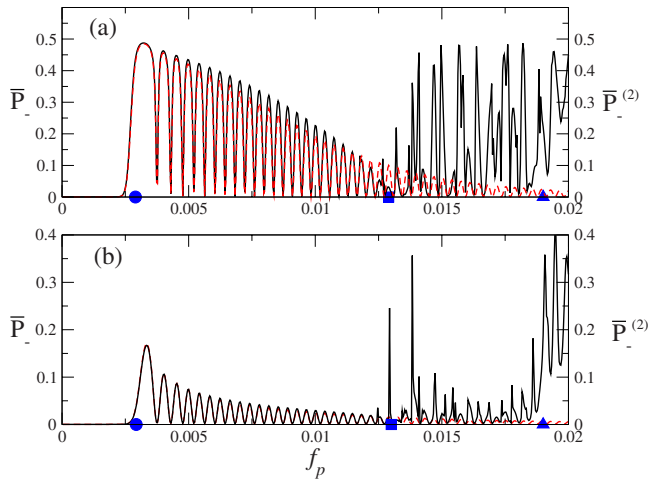

FIG. 7. (Color online) $\bar{P}_-$ (black solid line) calculated employing the lowest six levels and $\bar{P}_-^{(2)}$ (red dashed line) calculated employing the lowest two levels as a function of the driving amplitude. Calculations were done using $K=150-300$ and $M=1024$. (a) $\delta f=-0.00309$ and (b) $\delta f=-0.00308$. The circle, square, and triangle denote the beginning of the first diamond D1, the end of D1, and the beginning of the second diamond D2, respectively, for the present value of δf. See text for details.

two levels, $\bar{P}_-^{(2)}$, i.e., with $N_l=2$. In Fig. 7(b) we plot a case slightly different (slightly off $n=28$ resonance condition for the TLS in the fast driving regime), for $\delta f=-0.00308$, where $\bar{P}_-$ is clearly smaller. For small amplitudes, $\bar{P}_-$ is nicely followed by $\bar{P}_-^{(2)}$, that indeed reproduces quite accurately the interference patterns both on-resonance and off-resonance, in Figs. 7(a) and 7(b), respectively. However, for $f_p\gtrsim 0.01$ the departure of $\bar{P}_-^{(2)}$ from the actual behavior is notorious, even before the end of the first diamond D1. In addition, $\bar{P}_-^{(2)}\to 0$ reflecting the fact that higher levels besides the lowest two are populated as f_p increases.

Unlike its beginning, the end of D1 is not so sharply defined, showing a rather poor change in contrast. In the experiments of Ref. 15 the data show a larger reduction in contrast, due to fast relaxation through intrawell transitions. Furthermore, in the experiment is $\Delta_{10}\gg\Delta_{00}$ and the population transfer is dominated by the transition at the avoided crossing Δ_{10} with no explicit signatures of additional multiple passages through the extra avoided crossing Δ_{11} [see Fig. 1(c) in Ref. 15]. In our case we have verified that, although $\Delta_{10}=2\times 10^{-3}\gg\Delta_{00}=3\times 10^{-4}$ is roughly the same relation than in the Ref. 15, additional transitions at $\Delta_{11}=1\times 10^{-2}$ contribute to sustain the values of $\bar{P}_-$, resulting in an effective reduction in the contrast at the end of D1. It is plausible that in the experimental qubit,[15] a high value of Δ_{11} gives, unlike our case, a negligible transition probability at this avoided crossing.

Here, we find that despite the poor contrast in a highly coherent DJFQ, the end of the first diamond is quite identifiable at $f_{1e}^D\sim 0.013$, giving a value of $f_{10}^D=0.484$ in good agreement with the position of the second avoided crossing Δ_{10} obtained from the analysis of the spectrum depicted in Fig. 2. Thus, the boundaries of the first diamond give a rather

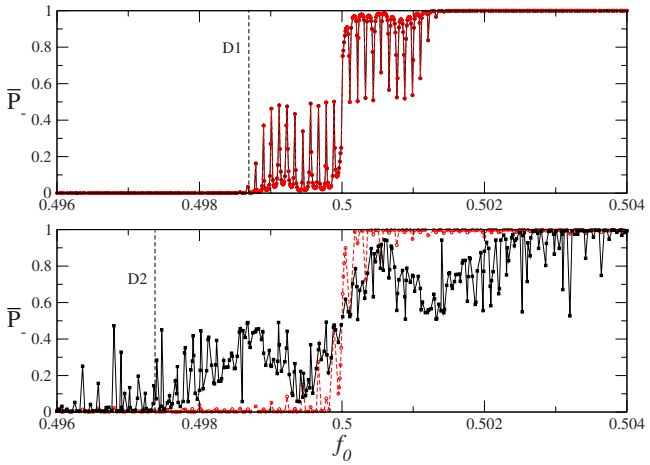

FIG. 8. (Color online) $\bar{P}_-$ (black solid line) as a function of the static flux f_0 for two different values of the driving amplitude f_p =0.001 (upper panel) and f_p=0.018 (lower panel) calculated using N_l=6. In both panels, a dashed line denotes the value of f_0 that for f_p=0.001 (f_p=0.018) gives the beginning of the first (second) diamond D1 (D2). As a comparison we plotted in red dashed line the $\bar{P}_-^{(2)}$ computed employing the lowest two levels. Numerical calculations were done with K=150–300 and M=1024. See Fig. 6 and text for further details.

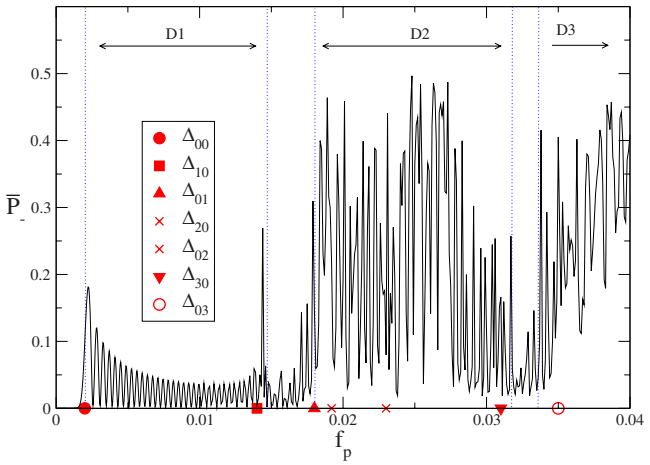

FIG. 9. (Color online) $\bar{P}_-$ for δf=−0.002 calculated employing the lowest eight levels as a function of the driving amplitude. Calculations were done using K=150–400 and M=1024. The red symbols in the axis show the values of f_p for which the different avoided crossings are reached (see Fig. 2). The vertical dotted lines indicate the borders of the different spectroscopic diamonds D1, D2, and D3.

satisfactory determination of the position of Δ_{00} and Δ_{10}, respectively.

For values of $f_p > 0.013$ the competition between the different transitions at the avoided crossings Δ_{00}, Δ_{10}, and Δ_{11}, turns the interpretation of the pattern followed by $\bar{P}_-$ rather complicated. However the beginning of the second diamond D2 at f_{2s}^D=0.019, gives the position of the avoided crossing Δ_{01}, at f_{01}^D=0.516 very close to the exact value (see Fig. 2).

In analogy with the experimental analysis,[15] the diamonds profiles can be studied in more detail for a given amplitude f_p and sweeping the flux detuning f_0. To this end, we select two vertical lines in Fig. 6 that correspond to f_p=0.001 and f_p=0.018, respectively.

In the upper panel of Fig. 8 we show $\bar{P}_-$ along f_p =0.001. A dashed line indicates the value f_0^{D1}=0.4988 at which the vertical line defined by f_p=0.001 intersects the lower edge of the D1 (see Fig. 6). As expected, the symmetry $\bar{P}_- \to 1-\bar{P}_-$ around f_0=0.5 holds. The profile of $\bar{P}_-$, sweeping the different equally spaced n resonances as f_0 changes, seems to be in very good agreement with the predicted TLS resonance pattern. Indeed we have included the results for $\bar{P}_-^{(2)}$ computed employing the lowest two levels, which are essentially superimposed to the actual $\bar{P}_-$. An estimate of the observed number of resonances obtained employing Eq. (7) is $n=[\epsilon_0/\omega]=[4\pi\alpha E_J S_{01}|\delta f|/\omega]$, being $[\cdots]$ the integer part. In this case is $|\delta f|=|0.5-f_0^{D1}|=0.00122$ and $4\pi\alpha E_J S_{01} \sim 9$. Thus for ω=0.001 we obtain n=11, which is exactly the number of maxima displayed in the upper panel of Fig. 8 for the selected range of flux detunings. Thus this analysis, complemented with the previous one performed in Fig. 7, confirms that close to the beginning of the first diamond D1, the TLS description is quite accurate.

The lower panel of Fig. 8 displays $\bar{P}_-$ for f_p=0.018 and the beginning of the second diamond D2 is indicated at f_0^{D2} =0.4974 by the vertical dashed line. The erratic pattern of resonances in $\bar{P}_-$ is in correspondence with the results presented in Fig. 7 for amplitudes inside the second diamond D2. As it occurred in that case, the competition between the transitions at different avoided crossings gives a profile of the occupation probability that strongly departs from a simple interference pattern as given by Eq. (7) and/or for the pattern displayed by $\bar{P}_-^{(2)}$.

Coming back to complete the spectroscopic analysis of Fig. 6, the end of the second diamond should be expected at $f_p \simeq 0.018$ corresponding to the position of the Δ_{20} avoided crossing. However, as it is easily checked from Fig. 6, we do not obtain the end of the second diamond for this value of f_p. Indeed D2 starts for a larger value of the amplitude. In our case $\Delta_{20} \sim 1 \times 10^{-7} \ll \Delta_{00}$ and therefore the transition probability $\propto \Delta_{20}^2/\omega f_{p4} \to 0$. As a consequence, the spectroscopic diamond contains no visible information on the avoided crossing Δ_{20}. This small gap should correspond to a crossing of transverse modes, which are not easily probed by the driving $f(t)$ which acts mainly along the longitudinal ϕ_l direction. Similar drawback for detecting transverse modes has been reported in the experiment.[15] A possible way to increase the resolution of this gap is to increase the transition probability by reducing the driving frequency ω. However, larger driving periods could be concomitant with the loss in resolution of the individual n resonances.[15]

Obtaining numerically the diamond pattern besides the beginning of the second one D2 is a formidable task, essentially due to the extremely large CPU needed. Figure 9 shows a cut of $\bar{P}_-$ for δf=−0.0020 up to amplitudes f_p ~0.04. For the larger amplitudes ($f_p > 0.02$), we needed to perform the calculations employing eight levels (N_l=8). For the small amplitudes the edges of the first diamond D1 and

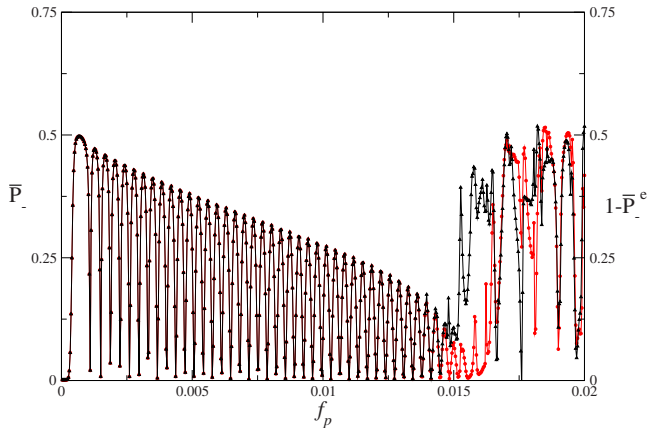

FIG. 10. (Color online) $\bar{P}_-$ (red line) and $1-\bar{P}_-^e$ (black line) as a function of the driving amplitude for $\delta f=-0.00066$. Calculations were done employing the lowest six levels using $K=150-300$ and $M=1024$.

the beginning of the second diamond D2 are clearly visible in the abrupt changes exhibited by $\bar{P}_-$. On the other hand, as we have already mentioned, no evidence of population transfer is obtained for the transverse avoided crossings Δ_{20} and Δ_{02}. For larger amplitudes, one can distinguish a region where $\bar{P}_-$ is small ($\bar{P}_- \lesssim 0.1$) as separating the end of the second diamond D2 and the beginning of the third diamond D3. In Fig. 9 we show the points in f_p where the avoided crossings at Δ_{30} (triangle down) and Δ_{03} (open circle) are reached.

IV. EXCITED-STATE AMPLITUDE SPECTROSCOPY

In this section we explore an alternative amplitude spectroscopic method to study the quantum dynamics of the DJFQ starting from a different initial condition. The gedanken experiment consist on preparing the system in the first excited state $|n=1,f_0\rangle$ for $f_0 \lesssim 0.5$. In this way, and depending on the value of f_0 chosen, the Δ_{00} or Δ_{10} avoided crossing could be reached first as the amplitude is increased. With this initial state, the time-averaged occupation probability is

$$\bar{P}_+^e = 1 - \bar{P}_-^e = \sum_{n,m=0}^{N_l-1} p_{nm}\Lambda_{nm}^e, \tag{28}$$

where

$$\Lambda_{nm}^e = \sum_{\beta=1}^{N_d}\sum_{k=-K}^{K} \langle n,k|\varphi_\beta\rangle\langle\varphi_\beta|1,0\rangle\langle 1,0|\varphi_\beta\rangle\langle\varphi_\beta|m,k\rangle.$$

If we compare with Eq. (27) we see that now $\bar{P}_+^e$ depends on the amplitude $\langle\varphi_\beta|1,0\rangle$ instead of $\langle\varphi_\beta|0,0\rangle$. In general, in highly coherent devices, one can define an average occupation probability $\bar{P}_+^{(s)}$ depending on the initial state $|s\rangle$, with the amplitude $\langle\varphi_\beta|s,0\rangle$ instead of $\langle\varphi_\beta|0,0\rangle$ in Eq. (27).

For values of $f_0 \lesssim 0.5$ and $f_p \to 0$ we have $\bar{P}_+=1$ ($\bar{P}_-=0$) and $\bar{P}_+^e=0$ ($\bar{P}_-^e=1$). In Fig. 10 we plot $\bar{P}_-$ and $1-\bar{P}_-^e$ as a function of the driving amplitude for a fixed value for the detuning ($\delta f=-0.00066$), such that the avoided crossing Δ_{00} is reached for smaller amplitudes than the Δ_{10}. For small values of f_p the system behaves as a TLS and both probabilities give the same information. As the driving amplitude is increased ($f_p \sim 0.015$) noticeable differences between $\bar{P}_-$ and $1-\bar{P}_-^e$ emerge. Indeed, in the highly coherent case the initial condition plays an important role in the quantum dynamics of the system already when approaching the second avoided crossing Δ_{10}.

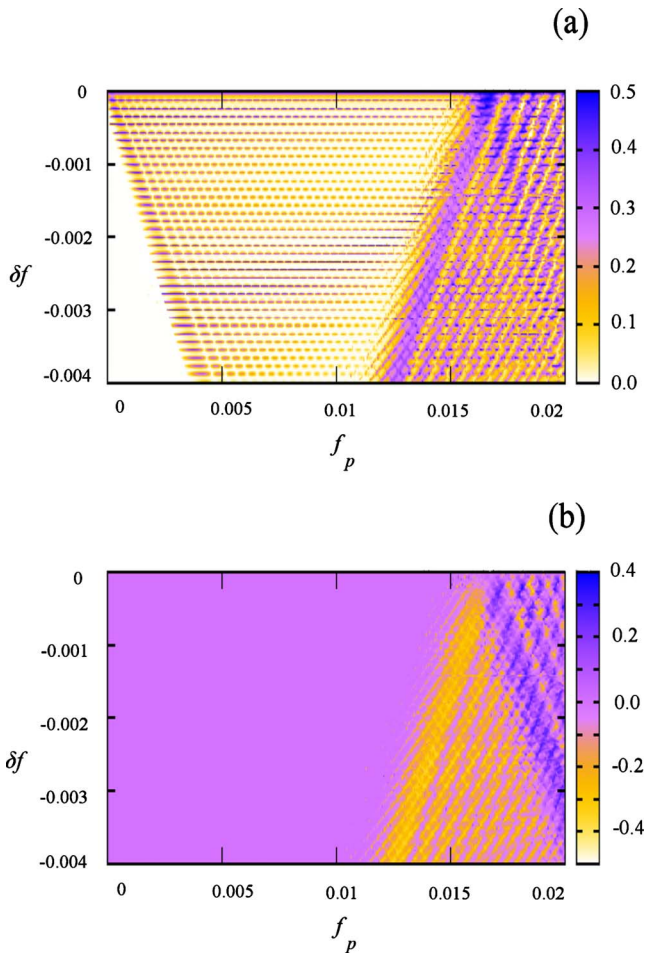

FIG. 11. (Color online) Large-amplitude excited-state spectroscopic (half) diamonds obtained for the DJFQ with $\eta=0.25$ and $\alpha=0.8$ at a driven frequency $\omega=0.001$. Calculations were done employing $N_l=6$ (six levels), $150 \leq K \leq 300$ and $M=1024$. (a) Intensity plot of $1-\bar{P}_-^e$. (b) Intensity plot of $\bar{P}_- - (1-\bar{P}_-^e)$.

In Fig. 11(a) we show the contour plot of $1-\bar{P}_-^e$ as a function of $(f_p,\delta f)$ for $\delta f<0$ and $\omega=0.001$. The range of values of f_p and δf and the grid are the same used to obtain the results showed in Fig. 6. By inspection of Figs. 6(a) and 11(a) we conclude that both amplitude spectroscopy methods give the same information before the Δ_{10} avoided crossing is reached. While the end of the first diamond D1 is determined with a good contrast with the excited-state amplitude spectroscopy method, the beginning of the second diamond D2 is still very difficult to determine.

In order to analyze the information hidden in the different spectroscopic diamonds we plot the difference between the

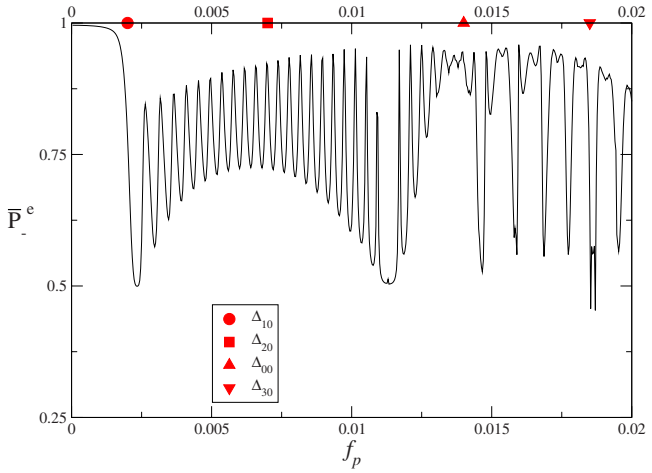

FIG. 12. (Color online) $\bar{P}_-^e$ calculated employing the lowest eight levels as a function of the driving amplitude for $\delta f=-0.014$. The system is driven at a frequency $\omega=0.001$, $K=150-300$ and $M=1024$. The red symbols show the position of the different avoided crossings.

probabilities used to construct the diamonds in Figs. 6(a) and 11(a). In Fig. 11(b) we show the contour plot of $\bar{P}_-+\bar{P}_-^e-1$ as a function of $(f_p,\delta f)$ for $\delta f<0$ and $\omega=0.001$. As we mentioned, the difference is zero for values of f_p such that the Δ_{10} is not reached. It is interesting to mention that now the end of the first diamond D1 and the beginning of D2 can be determined with a rather good contrast, due the cancellation of some intrincated interference patterns present in both $\bar{P}_-$ and $1-\bar{P}_-^e$.

Finally we evaluate the probability $\bar{P}_-^e$ as a function of the driving amplitude for a fixed value of the flux detuning close to the Δ_{10} avoided crossing. In this case $\bar{P}_-^e$ follows the TLS behavior up to the Δ_{10} avoided crossing but once the driving amplitude reaches the Δ_{00} additional levels should be included in order to properly describe the quantum dynamics of the DJFQ. In Fig. 12 we plot $\bar{P}_-^e$ for $f_0\sim f_{10}=0.484$, as a function of the driving amplitude up to values that drive the system close to the Δ_{30}, for which we have to employ eight levels in the numerical calculations. In the figure the changes in $\bar{P}_-^e$ reveal the position of the different avoided crossings allowing a clear detection of Δ_{10}, Δ_{00}, and Δ_{30}.

V. SUMMARY AND CONCLUSIONS

We have numerically solved the quantum dynamics of the device for the JFQ under strong harmonic driving in the fully coherent regime. Starting from the ground state we have studied the temporal evolution of the occupation probability and analyzed the spectroscopic diamonds obtained for the time-averaged occupation as a function of flux detuning and driving amplitudes. We have shown that for small amplitudes the description in terms of a TLS reproduces very well the observed pattern of Landau-Zener-Stückelberg interferences, as expected. On the other hand, the TLS description breaks down for driving amplitudes such that the avoided crossing Δ_{10} is reached. The spectroscopic diamonds exhibit in this case interference patterns with a rather complex structure, due to the coherent evolution among all coupled energy levels. This situation is different from the experiment of Ref. 15 where there is a higher contrast in the diamond patterns due to the intrawell relaxation and short coherence times. In spite of this, in the fully coherent regime explored in this work, we find that the edges of the diamonds clearly define the position of the different avoided crossings, as can be observed in Fig. 9, for example, even when the contrast is rather poor. In Sec. IV we have proposed a way to obtain further information in this case. In a highly coherent DJFQ it is possible to prepare the system in the first excited state, for example, with a π Rabi pulse. From there, the excited-state amplitude spectroscopy could be performed. A comparison of the occupation probabilities obtained from the ground-state amplitude spectroscopy and the excited-state amplitude spectroscopy, as performed in Fig. 11(b), can now bring good contrast for the resolution of the second diamond. In a perfectly coherent closed system one could continue even further, performing another amplitude sweep starting from the second excited state, compare it with the results obtained starting from the first excited state, and so on. Of course, in a real system the possibility of these "excited-state amplitude spectroscopies" will be strongly limited by decoherence and relaxation processes. In current highly coherent DJFQ (with dephasing times on the order of 1 μs) the first excited-state amplitude spectroscopy seems to be feasible. In this case, this could give an important indication of the coherence of the device as wells as additional and complementary information of the multilevel structure of the energy spectrum of DJFQ.

ACKNOWLEDGMENTS

We acknowledge discussions with Sergio Valenzuela. We also acknowledge financial support from CNEA, CONICET (Grants No. PIP11220080101821 and No. PIP11220090100051) and ANPCyT (Grants No. PICT2006-483 and No. PICT2007-824).

[1] Y. Nakamura, Y. A. Pashkin, and J. S. Tsai, Nature (London) **398**, 786 (1999).

[2] J. E. Mooij, T. P. Orlando, L. S. Levitov, L. Tian, C. H. van der Wal, and S. Lloyd, Science **285**, 1036 (1999); T. P. Orlando, J. E. Mooij, L. Tian, C. H. van der Wal, L. S. Levitov, S. Lloyd, and J. J. Mazo, Phys. Rev. B **60**, 15398 (1999).

[3] D. Vion, A. Aassime, A. Cottet, P. Joyez, H. Pothier, C. Urbina, D. Esteve, and M. H. Devoret, Science **296**, 886 (2002).

[4] J. M. Martinis, S. Nam, J. Aumentado, and C. Urbina, Phys. Rev. Lett. **89**, 117901 (2002); Y. Yu, S. Han, X. Chu, S.-I. Chu, and

Z. Wang, Science **296**, 889 (2002).
[5] Y. Makhlin, G. Schön, and A. Shnirman, Rev. Mod. Phys. **73**, 357 (2001); G. Wendin and V. Shumeiko, Low Temp. Phys. **33**, 724 (2007).
[6] I. Chiorescu, Y. Nakamura, C. J. P. M. Harmans, and J. E. Mooij, Science **299**, 1869 (2003).
[7] I. Chiorescu, P. Bertet, K. Semba, Y. Nakamura, C. J. P. M. Harmans, and J. E. Mooij, Nature (London) **431**, 159 (2004); E. Il'ichev, N. Oukhanski, A. Izmalkov, Th. Wagner, M. Grajcar, H.-G. Meyer, A. Yu. Smirnov, A. Maassen van den Brink, M. H. S. Amin, and A. M. Zagoskin, Phys. Rev. Lett. **91**, 097906 (2003); Y. Yu, D. Nakada, J. C. Lee, B. Singh, D. S. Crankshaw, T. P. Orlando, W. D. Oliver, and K. K. Berggren, *ibid.* **92**, 117904 (2004); A. Lupaşcu, C. J. M. Verwijs, R. N. Schouten, C. J. P. M. Harmans, and J. E. Mooij, *ibid.* **93**, 177006 (2004); P. Bertet, I. Chiorescu, G. Burkard, K. Semba, C. J. P. M. Harmans, D. P. DiVincenzo, and J. E. Mooij, *ibid.* **95**, 257002 (2005).
[8] F. Yoshihara, K. Harrabi, A. O. Niskanen, Y. Nakamura, and J. S. Tsai, Phys. Rev. Lett. **97**, 167001 (2006); K. Kakuyanagi, T. Meno, S. Saito, H. Nakano, K. Semba, H. Takayanagi, F. Deppe, and A. Shnirman, *ibid.* **98**, 047004 (2007).
[9] E. N. Pozzo and D. Domínguez, Phys. Rev. Lett. **98**, 057006 (2007).
[10] E. N. Pozzo, D. Domínguez, and M. J. Sánchez, Phys. Rev. B **77**, 024518 (2008).
[11] A. Ferrón and D. Dominguez, Phys. Rev. B **81**, 104505 (2010).
[12] A. Izmalkov, M. Grajcar, E. Il'ichev, N. Oukhanski, Th. Wagner, H.-G. Meyer, W. Krech, M. H. S. Amin, A. Maassen van den Brink, and A. M. Zagoskin, Europhys. Lett. **65**, 844 (2004).
[13] W. D. Oliver, Y. Yu, J. C. Lee, K. K. Berggren, L. S. Levitov, and T. P. Orlando, Science **310**, 1653 (2005); D. M. Berns, W. D. Oliver, S. O. Valenzuela, A. V. Shytov, K. K. Berggren, L. S. Levitov, and T. P. Orlando, Phys. Rev. Lett. **97**, 150502 (2006).
[14] A. Izmalkov, S. H. W. van der Ploeg, S. N. Shevchenko, M. Grajcar, E. Il'ichev, U. Hbner, A. N. Omelyanchouk, and H.-G. Meyer1, Phys. Rev. Lett. **101**, 017003 (2008).
[15] D. M. Berns, M. S. Rudner, S. O. Valenzuela, K. K. Berggren, W. D. Oliver, L. S. Levitov, and T. P. Orlando, Nature (London) **455**, 51 (2008); W. D. Oliver and S. O. Valenzuela, Quantum Inf. Process. **8**, 261 (2009).
[16] M. S. Rudner, A. V. Shytov, L. S. Levitov, D. M. Berns, W. D. Oliver, S. O. Valenzuela, and T. P. Orlando, Phys. Rev. Lett. **101**, 190502 (2008).
[17] S. N. Shevchenko, S. Ashhab, and F. Nori, Physics Report **492**, 1 (2010).
[18] X. Wen and Y. Yu, Phys. Rev. B **79**, 094529 (2009).
[19] For example, in Ref. 8 is $T_2 \sim 1$ μs while in Ref. 15 is $T_2 \sim 20$ ns.
[20] G. Floquet, Ann. Sci. Ec. Normale Super. **12**, 47 (1883).
[21] S.-K. Son, S. Han, and Shih-I. Chu, Phys. Rev. A **79**, 032301 (2009).
[22] S.-I. Chu and D. A. Telnov, Phys. Rep. **390**, 1 (2004); D. A. Telnov and Shih-I. Chu, Phys. Rev. A **71**, 013408 (2005); S. Kolher, J. Lehmann, and P. Hänggi, Phys. Rep. **406**, 379 (2005); J. H. Shirley, Phys. Rev. **138**, B979 (1965).
[23] S. K. Son and Shih-I. Chu, Phys. Rev. A **77**, 063406 (2008).
[24] F. G. Paauw, A. Fedorov, C. J. P. M. Harmans, and J. E. Mooij, Phys. Rev. Lett. **102**, 090501 (2009).
[25] Y. Shimazu, Y. Saito, and Z. Wada, J. Phys. Soc. Jpn. **78**, 064708 (2009).
[26] S. Ashhab, J. R. Johansson, A. M. Zagoskin, and F. Nori, Phys. Rev. A **75**, 063414 (2007).
[27] C. Zener, Proc. R. Soc. London, Ser. A **137**, 696 (1932).
[28] M. D. Feit, J. A. Fleck, and A. Steiger, J. Comput. Phys. **47**, 412 (1982).